









## Research Article

# An Electromechanical Impedance-Based Imaging Algorithm for Damage Identification of Chemical Milling Stiffened Panel

Xie Jiang <sup>1</sup>, Wensong Zhou <sup>2</sup>, Xize Chen <sup>2</sup>, Xin Zhang <sup>3</sup>, Jiefeng Xie <sup>4</sup>, Tao Tang <sup>1</sup>,  
Yuxiang Zhang <sup>1</sup> and Zhengwei Yang <sup>1</sup>

<sup>1</sup>PLA Rocket Force University of Engineering, Xi'an 710025, China

<sup>2</sup>School of Civil Engineering, Harbin Institute of Technology, Harbin 150090, China

<sup>3</sup>Northwest Institute of Nuclear Technology, Xi'an 710024, China

<sup>4</sup>South China University of Technology, Guangzhou 510641, China

Correspondence should be addressed to Xin Zhang; rfue00@163.com and Zhengwei Yang; yangzhengwei1136@163.com

Received 8 December 2023; Revised 6 April 2024; Accepted 23 April 2024; Published 17 May 2024

Academic Editor: Francesc Pozo

Copyright © 2024 Xie Jiang et al. This is an open access article distributed under the Creative Commons Attribution License, which permits unrestricted use, distribution, and reproduction in any medium, provided the original work is properly cited.

The multiple intersecting stiffeners on the chemical milling stiffened panel (CMSP) limit the application of active health monitoring methods on it. An imaging algorithm based on electromechanical impedance (EMI) and probability-weighting is proposed to achieve quantitative evaluation and localization of the damage on CMSP. The proposed algorithm compensates for the difference in sensor performance with coefficients and there is no need to determine the key parameters of the algorithm through prior experiments. In the paper, the applicability of ultrasonic guided wave (GW) and EMI on CMSP was first studied through the finite element method. Based on EMI and the mean absolute percentage deviation (MAPD), the selected damage indicator (DI), a probability-weighted damage imaging algorithm are proposed and experimentally verified. The results indicate that due to the reflection and attenuation effects of stiffeners on GW, the signal characteristics of damage scattering waves are contaminated, making it difficult to quantitatively characterize the damage from GW signals through DIs. MAPD is positively correlated with the damage degree and has consistency in characterizing the signal of different PZTs under the same working condition. The feasibility and accuracy of the proposed algorithm are verified through experiments which show a strong engineering application capability.

## 1. Introduction

Stiffened structures have been widely used in commercial aircraft, satellites, launch vehicles, and other aerospace fields for their advanced structural performance such as excellent load-bearing capacity [1–3]. The initial defects of the stiffened panel accumulate and expand when the launch vehicle is under various loads which greatly endanger the safety of personnel and equipment. Thus, it is important and meaningful to study the online damage monitoring method for stiffened panels.

GW is a common active structural health monitoring (SHM) technology [4, 5]. There have been many studies on the propagation law of GW in the stiffened panel. Ricci et al. [6] studied the effectiveness of the A0 mode in detecting

delamination and debonding in stiffened composite plates with finite thickness and infinite lateral dimensions through theoretical analysis, numerical modeling, and experimental study. Ramadas et al. [7] explored the interaction between A0 mode and structural discontinuities in composite structures and verified the back-propagation of “turning mode” from the thin region to the spar web through numerical simulation and experiment. Faisal Haider et al. [8] considered two cases of plate and proposed an effective global-local analysis method to determine Lamb wave scattering from a discontinuity. Reusser et al. [9] established a simple explanatory model for the scattering of low-order Lamb waves crossing a stiffener which illuminates the underlying mechanics. They also concluded that stop-bands for transmission of longitudinal pressure waves across

a stiffener line up with flexural resonances of the stiffener. Bijudas et al. [10] studied three damage cases of disbonding of stiffeners from the base plate, and vertical and embedded cracks in the stiffened plate. They conducted baseline-free damage experiments based on time reversal Lamb waves (TRLW), and the results showed that TRLW had a good recognition performance on stiffened panels with one single stiffener. Schaal and Mal [11] used an analytical approach to solve the benchmark problem of Lamb wave reflection at a free end as well as the interaction of Lamb waves with upward and downward step discontinuities. The analytically derived results show a good agreement with the transient finite element simulations. Currently, the studies of GW in complex structures mainly focus on the propagation mechanisms. The capacity of GW for actual damage identification of stiffened panels is still unknown.

As another active SHM technology, EMI has a wide range of applications in different structures due to its low cost, high sensitivity to minor damage, and the potential to provide real-time, remote, and autonomous monitoring [12, 13]. Wu et al. [14] monitored the bolted connections based on the wearable piezoelectric ring and EMI, using two statistical indicators: MAPD and the root mean square deviation (RMSD) to achieve a quantitative evaluation of bolt looseness. Du et al. [15] constructed a convolutional neural network (CNN) for multitask which consists of a temperature compensation subnetwork and a lightweight damage identification subnetwork. The model achieves monitoring of bolt loosening in temperature-varying environments. Ai and Cheng [16] splitted the electromechanical admittance (EMA) signatures of concrete into multiple subrange responses and selected the maximum index as the training input of the two-dimensional (2D) CNN. The constructed model achieved rapid prediction of the damage severity of concrete structures. Li et al. [17] validated that conductance resonant frequency decreases while conductance resonant peak increases with the increase of concrete compressive strength after analyzing the collected data. The linear regression-CNN hybrid model shows a good performance in the prediction of concrete strength development. Ai et al. [18] proposed a modern structural damage detection (SDD) method that uses one-dimensional (1D) CNN to automatically learn raw EMA features. The SDD is used for identifying minor/severe quality losses and bolt loosening damage in concrete structures. Fu et al. [19] proposed a cloud-based wireless impedance monitoring system for corrosion detection of small-diameter pipelines which comprises a smart corrosion sensing node and a wireless impedance monitoring system. Zhu et al. [20] proposed an approach that combines data expansion, series-to-image conversion, and an intelligent model to predict the external impact energy of sandwich composite materials. Although EMI has been employed in many structures, there are still few reports on its application research on stiffened panels.

Stiffened panel is usually processed into a grid form by chemical milling, mechanical milling, or casting. The stiffened panel studied in the paper is the CMSP which contains

multiple stiffeners that are perpendicular to each other, and there is a rounded structure at the junction of the stiffener and the base plate that is equivalent in thickness to the stiffener. This paper first explores the applicability of GW and EMI for CMSP damage characterization. Then, four DIs are used to quantitatively characterize the signals of EMI under five damage severities. After comparison, the DI with good characterization effects is determined. It is taken as a parameter of the proposed modified probability-weighted algorithm to further localize the damage on CMSP.

## 2. The Detection Foundation of the EMI Method

*2.1.  $d_{31}$ -Type Piezoelectric Wafers.* The piezoelectric material of the PZT is lead zirconate titanate (PbZr(Ti)O<sub>3</sub>), a ferroelectric ceramic that attains a permanently polarized state when it is poled. For a small variation in the electric field, it behaves approximately linearly near that state, which can be expressed by the following linear piezoelectric equations [21]:

$$\begin{aligned}\varepsilon_{ij} &= c'_{ijkl}\sigma_{kl} + d_{kij}E_k, \\ D_i &= d_{ikl}\sigma_{kl} + \varepsilon_{ik}^T E_k,\end{aligned}\quad (1)$$

where  $\varepsilon_{ij}$  is the strain tensor,  $D_i$  is the electric displacement component,  $\sigma_{kl}$  is the stress tensor, and  $E_k$  is the electric field.  $c'_{ijkl}$ ,  $d_{kij}$ , and  $\varepsilon_{ik}^T$  denote the inverse elastic, piezoelectric, and dielectric constants, respectively. The electric constants matrix has only three independent piezoelectric coefficients,  $d_{31}$ ,  $d_{33}$ , and  $d_{15}$  as the poled piezoelectric ceramic is an orthotropic material with a plane of symmetry whose normal is in the poled direction. The other coefficients in the matrix are all zero as follows:

$$d_{ij} = \begin{bmatrix} 0 & 0 & 0 & 0 & d_{15} & 0 \\ 0 & 0 & 0 & d_{24} & 0 & 0 \\ d_{31} & d_{32} & d_{33} & 0 & 0 & 0 \end{bmatrix}. \quad (2)$$

In the matrix,  $d_{31} = d_{32}$  and  $d_{24} = d_{15}$ . The PZT which is made of this piezoelectric ceramic is named as the  $d_{31}$ -type piezoelectric wafer. The piezoelectric constant matrix of the PZT used in this paper is as follows:

$$d_{ij} = \begin{bmatrix} 0 & 0 & 0 & 0 & 5.84 & 0 \\ 0 & 0 & 0 & 5.84 & 0 & 0 \\ -2.1 & -2.1 & 5 & 0 & 0 & 0 \end{bmatrix} \times 10^{-10} \text{C/N}. \quad (3)$$

*2.2. Principle of the EMI.* Yang et al. [22] proposed and simplified the coupling system between PZT and the host structure into a 2D plane model and the model is adopted in the paper since it is more consistent with the experimental results [23]. The analysis of the 2D structure takes the inertial forces in two directions of the PZT into consideration which makes the solution of the admittance closer to the real situation. The admittance obtained is expressed in the following equations:

$$Y(\omega_p) = \frac{j\omega_p}{h_p} \left\{ \frac{\bar{Y}_p^E}{1 - \mu_p^2} \left[ \begin{array}{l} (d_{31} + \mu_p d_{32}) \left( 2Ab_p \tan \frac{K_p a_p}{2} - d_{31} a_p b_p \right) \\ + (\mu_p d_{31} + d_{32}) \left( 2Ca_p \tan \frac{K_p b_p}{2} - d_{32} a_p b_p \right) \end{array} \right] + \bar{\epsilon}_{33}^T a_p b_p \right\}, \quad (4)$$

$$\begin{Bmatrix} A_p \\ C_p \end{Bmatrix} = \mathbf{N}^{-1} \begin{Bmatrix} d_{31} \\ d_{32} \end{Bmatrix}, \quad (5)$$

$$\mathbf{N} = \mathbf{I} - \frac{j\omega_p}{\bar{Y}_p^E K_p h_p} \begin{bmatrix} \frac{Z_{11}}{b_p} - \frac{Z_{21}\mu_p}{a_p} & \frac{Z_{12}}{b_p} - \frac{Z_{22}\mu_p}{a_p} \\ -\frac{Z_{11}\mu_p}{b_p} + \frac{Z_{21}}{a_p} & -\frac{Z_{12}\mu_p}{b_p} + \frac{Z_{22}}{a_p} \end{bmatrix} \times \begin{bmatrix} -\tan \frac{k_p a_p}{2} & 0 \\ 0 & -\tan \frac{k_p b_p}{2} \end{bmatrix}, \quad (6)$$

where  $Y(\omega_p)$  is the admittance;  $j$  is  $(-1)^{1/2}$ ;  $\omega_p$  denotes the excitation angular frequency at work;  $\mu_p$  is the Poisson's ratio of the sensor;  $b_p$ ,  $a_p$ , and  $h_p$  are the length, width, and thickness of the PZT, respectively;  $\bar{\epsilon}_{33}^T$  is the complex dielectric constant at constant stress and  $\bar{\epsilon}_{33}^T = \epsilon_{33}^T (1 - j\delta)$ , where  $\epsilon_{33}^T$  is the dielectric constant;  $\delta$  denotes the dielectric loss factor;  $\bar{Y}_p^E = Y_p^E (1 + j\eta)$  represents the complex Young's modulus of PZT at the zero-elastic field and  $Y_p^E$  is the real Young's modulus;  $\eta$  is the mechanical loss factor;  $d_{31}$  and  $d_{32}$  are both piezoelectric constants;  $K_p = \omega \sqrt{\rho_p / \bar{Y}_p^E}$  denotes the wave number;  $\rho_p$  is the mass density of the sensor;  $A_p$  and  $C_p$  are the unknown coefficients determined from the boundary conditions. For a certain system, the above parameters are fixed values.  $\mathbf{I}$  is the identity matrix of  $2 \times 2$ ;  $Z_{11}$  and  $Z_{22}$  are the direct force impedances;  $Z_{12}$  and  $Z_{21}$  represent the cross impedances. Since the condition of PZT and adhesive layers usually remains unchanged, the admittance of the three-layer piezoelectric intelligent structure (containing PZT, adhesive layers, and the host structure) can reflect the structure status through signal change.

To detect damage with EMI, the PZT needs to be coupled on the surface of the host structure and then applied with AC voltage. Due to the inverse piezoelectric effect, the PZT undergoes deformation and drives the host structure to vibrate together. Similarly, the vibration of structure will react on the PZT, causing its deformation. An electrical response will be generated due to the positive piezoelectric effect of PZT. Then, the current signal is extracted and analyzed in an impedance analyzer. By comparing the impedance curves, the damage information of the tested structure can be inferred. The EMI measuring system is shown in Figure 1.

### 3. Numerical Study on PZT Structure Interaction

**3.1. Simulation Setup.** The CMSP is modeled by Solid185 elements whose length and width are both 295 mm. Eight  $d_{31}$  PZTs ( $\Phi 8 \text{ mm} \times 2 \text{ mm}$ ) are arranged on the CMSP surface as

shown in Figure 2(a) and are numbered 1#–8# in a clockwise direction. The PZTs are bonded to the CMSP and the coupling between the PZT and the structure is shown in the locally enlarged image in Figure 2(a). The cross-sectional diagram of the stiffener is shown in Figure 2(b). The width of the stiffener  $W$  is 7 mm and the panel thickness  $H_1$  is 4 mm. The stiffener thickness  $H_2$  and the fillet radius  $R_s$  are equal, both of which are 10 mm. The material of CMSP is 2219 aluminum alloy, with a density of  $2840 \text{ kg/m}^3$ , an elastic modulus of 73.1 GPa, and a Poisson's ratio of 0.33.

Based on the PZT coupled with the structure, GW and EMI, the two detection methods, can be used for CMSP health monitoring. As the mechanisms and characteristics of these two technologies are different, the applicability of the GW and EMI on CMSP are separately studied as follows.

**3.2. Damage Quantification Effect Based on GW.** To excite GW in CMSP, a five-cycle sinusoid tone-burst signal enclosed in a Hanning window is applied to PZT. 150 kHz is selected as the excitation center frequency  $f_c$  to ensure the accuracy of damage identification. CMSP is divided into multiple regional units by vertical and horizontal stiffeners. To visually observe the GW propagation in the structure, an excitation signal was applied to 1# PZT in the simulation. The time step is set to  $1/(10f_c)$  and a total of 250 data points were collected within the range of 0–167  $\mu\text{s}$ . The total displacement of CMSP at 37  $\mu\text{s}$ , 85  $\mu\text{s}$ , and 110  $\mu\text{s}$  is shown in Figures 3(a)–3(c).

As shown in Figure 3(a), GW propagates uniformly around the center of 1# PZT in the initial stage of propagation. The propagation energy of GW varies in different directions since the angles between the stiffeners and the wavefront are not constant. For those stiffeners parallel to the wavefront, the wave exhibits better passability. Figure 3(b) shows that there is no clear wavefront at 85  $\mu\text{s}$  because there occurs GW reflection and mode conversion at the stiffeners. From Figure 3(c), it can be concluded that GW can still cover the entire CMSP although the stiffeners attenuate its propagation energy.

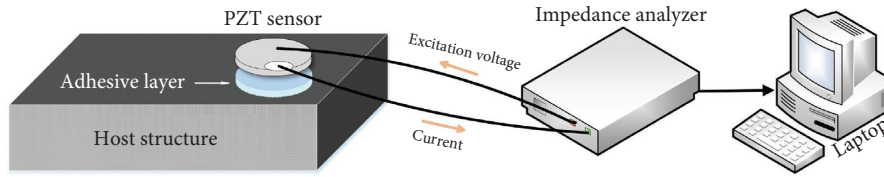


FIGURE 1: Schematic demonstration of the EMI measuring system.

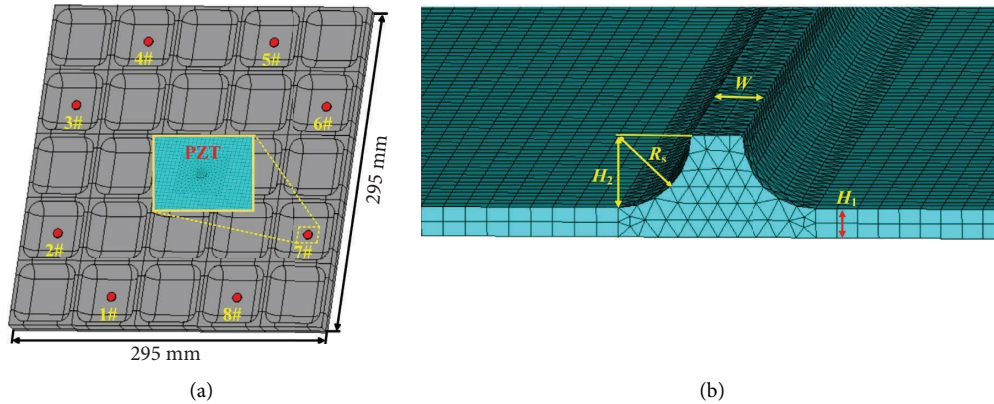


FIGURE 2: Schematic of (a) the CMSP and PZTs' layout and (b) the cross-section of one stiffener.

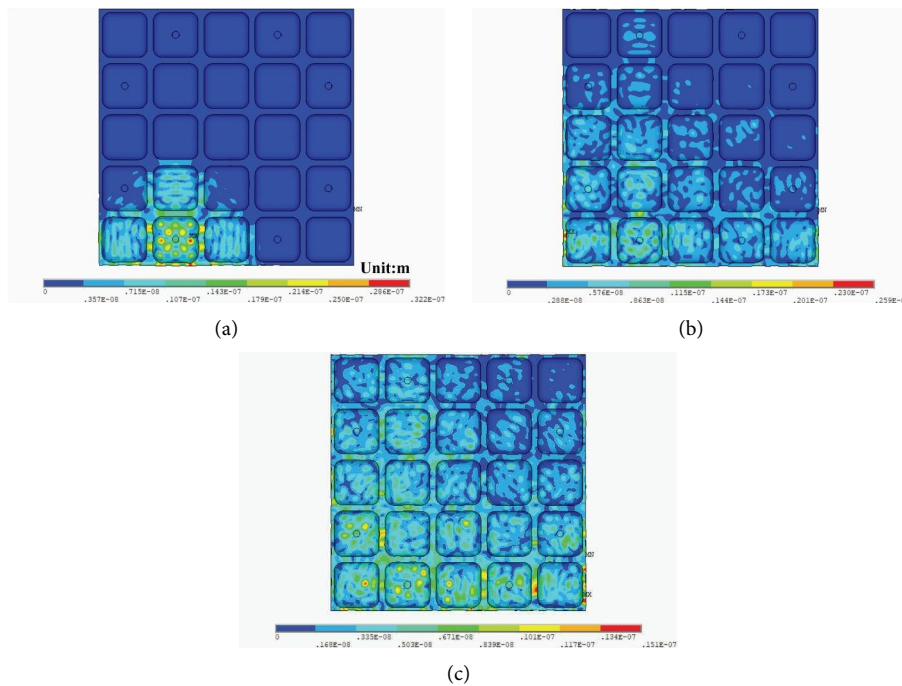


FIGURE 3: The propagation of GW at (a) 37  $\mu$ s, (b) 85  $\mu$ s, and (c) 110  $\mu$ s.

For complex structures such as CMSP, GW reflection and mode conversion occur at the stiffeners. The different propagation speeds of different modes will lead to wave packet aliasing and decrease the interpretability of the signal which makes it difficult to extract damage scattering wave from the directly received signal [24]. The benchmark detection strategy [25] is often used for GW-based damage identification. It obtains the benchmark signal of the

structure in a non-destructive state and then subtracts the detection signal from the benchmark. The obtained residual signal is mainly the scattering wave generated from the damage. Further, information on the damage's location and size can be acquired after analyzing the residual signal with evaluation methods. As the stiffeners have adverse effects on wave propagation, it is difficult to extract damage information from the raw signals. Thus, the benchmark

strategy is adopted for damage detection in this section. To explore the GW's capacity of damage severity quantification, five different degrees of damage were studied in the simulation and they were set in sequence in the center of the CMSP by deleting elements. The specific parameters of the damages are illustrated in Table 1. Taking Condition 5# as an example, the damage setting diagram is shown in Figure 4. Figure 5 displays the GW collected by four PZTs under healthy and five damage conditions.

Figures 5(a)–5(d) represent the signals collected by 2#, 4#, 6#, and 8# PZT after excitation of 1# PZT, respectively. The projection on the Z0Y plane in each figure represents the superposition of the signals under each working condition. It can be seen that in all four PZTs signals, the wave packets are difficult to distinguish from each other since the GW undergoes mode conversion at the stiffener, and the extracted signal includes not only the direct wave but also the reflected waves from the stiffeners and boundary. The mixing of various modes makes it very difficult to directly observe the damage scattering signal. Wave packets with smaller amplitude are observed in the first half of the signal of 6# PZT (as shown in the dashed area in Figure 5(c)). This is because some GWs experienced significant energy attenuation after passing through multiple stiffeners on the path from 1# PZT to 6# PZT. 8# PZT and 6# PZT have the highest and lowest signal amplitude, respectively. The range of the signal of 2# PZT and 4# PZT is  $[-1, 1]$ . Comparing 2# PZT and 8# PZT, a conclusion can be drawn that the more stiffeners the GW crosses, the greater the attenuation of its propagation energy. The amplitude of the signal in Figures 5(a) and 5(b) illustrates that different part of the CMSP has different effects on the propagation of GW. When propagating from 1# PZT to 4# PZT, GW needs to pass through four stiffeners which are parallel to its propagation. While it only crosses one intersection of stiffeners from 1# PZT to 2# PZT. It seems that the transmission wave still retains relatively high energy after GW crossing through the stiffener parallel to its propagation. The projection on the Z0Y shows that the signal characteristics under each damage condition are not significantly different from the benchmark. To further quantify the signal differences, four common DIs were used in this paper, including RMSD [26], MAPD [27], the covariance (Cov) [28], and the correlation coefficient (CC) [29]. The DIs are expressed as follows:

$$\text{RMSD} = \sqrt{\frac{\sum_{i=1}^K (V_i - V_i^0)^2}{\sum_{i=1}^K (V_i^0)^2}}, \quad (7)$$

$$\text{MAPD} = \sum_{i=1}^K \left| \frac{V_i - V_i^0}{V_i^0} \right|, \quad (8)$$

$$\text{Cov} = \sum_{i=1}^K (V_i - \bar{V}) \cdot (V_i^0 - \bar{V}^0), \quad (9)$$

$$\text{CC} = \frac{1}{\sigma_V \sigma_{V^0}} \sum_{i=1}^K (V_i - \bar{V}) \cdot (V_i^0 - \bar{V}^0), \quad (10)$$

where  $K = 250$  represents the signal length,  $V_i^0$  and  $V_i$  denote the voltage amplitude of the  $i^{\text{th}}$  sample point before and after damage,  $\bar{V}^0$  and  $\bar{V}$  are the average voltage amplitude before and after damage,  $\sigma_{V^0}$  and  $\sigma_V$  represent the standard deviation before and after damage, respectively. The value of each DI has been normalized according to their respective maximum and the DIs of 2#–8# PZT under five damage conditions are shown in Figure 6.

It proves that the DIs are effective when they show a monotonically increasing or decreasing change as the damage degree gradually increases. However, taking the MAPD at 7# PZT as an example, it does not exhibit a monotonic pattern of change. Besides, for the same five damage conditions, even if the same DI is used, the rules between the DI and the damage degree at different PZTs are various. The reason for the poor indication of DIs is that the damage features contained in the GW are destroyed when the damage scattering wave passes through multiple perpendicular stiffeners. In the simulation, there is no noise interference in the signal and the damage set is a square region with obvious reflection boundaries around it. For the actual detection environment of stress corrosion cracks in CMSP, GW will be even more unable to meet the requirements for quantitative characterization of defects. Therefore, it is not feasible to use GW with conventional DIs to evaluate the degree of damage in CMSP.

**3.3. Harmonic Response Analysis of the Host Structure Coupled with PZT.** When using PZT for EMI, the selection of the starting and ending frequencies of the excitation will directly affect the identification results. Therefore, it is necessary to determine the frequency range sensitive to structural damage before the experiment. Within the targeted frequency range, the peaks and valleys on the admittance are often more obvious and the curve fluctuates greatly. The scanning signal should be first set within a larger frequency range. After determining the targeted range, the admittance signals of different working conditions are analyzed and compared within that range. When conducting harmonic response analysis on PZT coupled to the structure, a resonant alternating voltage signal  $\{v(t) = \bar{V}e^{j\omega_p t} \bar{V} = |V|e^{j\varphi_1}\}$  is applied to the upper surface of the PZT thickness direction, where the voltage amplitude is  $|V| = 1$  V and  $\omega_p = 2\pi f$ ,  $f$  is the excitation frequency, and the initial phase is  $\varphi_1 = 0$ . At the same time, 0 V is applied to the lower surface. The scanning frequency is set to 50 kHz–1 MHz and the sample point is 1600. The “FULL” method is taken as the solution method and “SPARSE” is taken as the equation solver in the finite element simulation. Then, we extract the surface charge of the PZT and calculate the admittance combined with the known excitation voltage and frequency. The expression is as follows:

$$Y = \frac{i(t)}{v(t)} = \frac{\partial Q_p / \partial t}{v(t)} = j2\pi f \frac{Q_p}{v(t)}, \quad (11)$$

TABLE 1: The specific parameters of the damages.

	Condition1#	Condition2#	Condition3#	Condition4#	Condition5#
Damage size (Length $\times$ Width $\times$ Depth)	2 mm $\times$ 2 mm $\times$ 0.4 mm	4 mm $\times$ 4 mm $\times$ 0.8 mm	6 mm $\times$ 6 mm $\times$ 1.2 mm	8 mm $\times$ 8 mm $\times$ 1.6 mm	10 mm $\times$ 10 mm $\times$ 2 mm

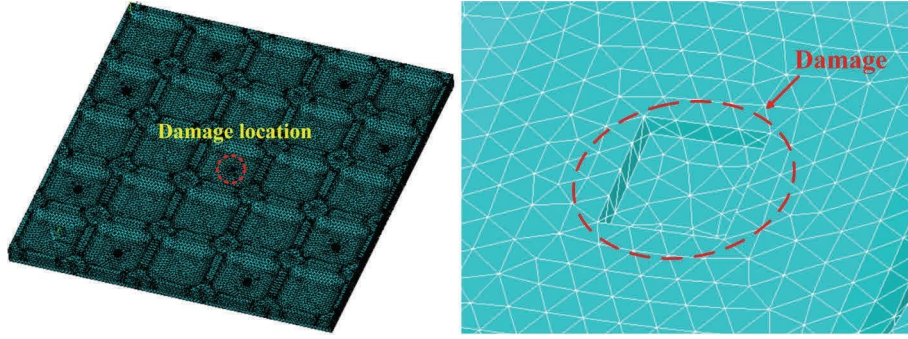


FIGURE 4: Schematic of the damage setting.

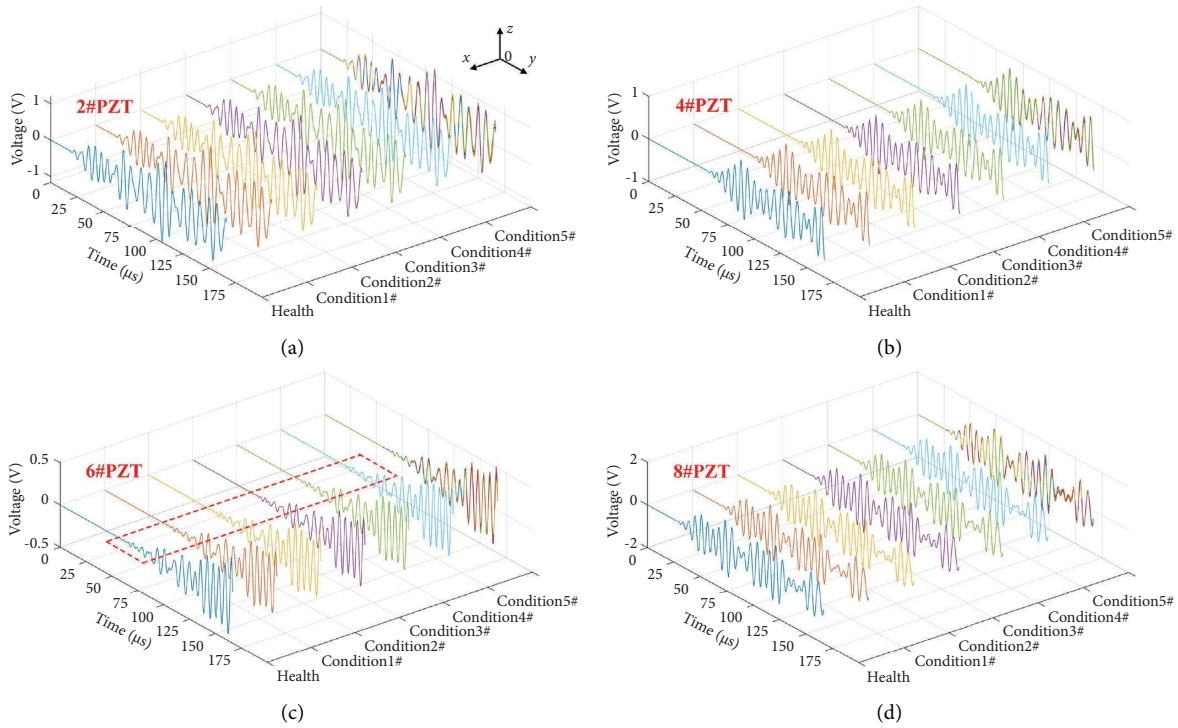


FIGURE 5: GW signals of sensors under different working conditions.

where  $Q_p$  is the surface charge of the PZT and  $i(t) = j\omega Q_p e^{j\omega_p t}$  is the current formed. The conductance (real part of the admittance) and the susceptance (imaginary part of the admittance) are shown in Figure 7.

In Figure 7, there are obvious extreme values in the conductance and the susceptance spectra in zone 1 and zone 2, with a frequency range of 110 kHz–160 kHz for zone 1. It should be considered that in most experiments, 30 kHz–400 kHz is commonly used as the excitation frequency because it is sensitive enough to detect small changes in structural integrity [30]. Meanwhile, due to the relatively dense resonant frequency of PZT around 150 kHz, 110 kHz–160 kHz was determined as the testing frequency range for subsequent experiments.

The CMSP model is the same as the one in Section 3.2 and there are 1200 sample points in the frequency range of 110 kHz–160 kHz. The extracted 1# PZT admittance under healthy conditions and condition 1 #–5# are shown in

Figure 8(a). The DIs calculated by replacing the voltage in equations (7)–(10) with the conductance are shown in Figure 8(b). From Figure 8, it can be seen that as the severity of damage deepens, all four DIs show varying degrees of change, with RMSD and MAPD being significantly positively correlated with the damage degree. Cov and CC are not able to characterize the relative magnitude of damage. Comparing the damage indication effects of Figures 6 and 8, a conclusion can be drawn that EMI has a stronger ability to characterize CMSP damage compared to GW since the admittance in EMI is directly related to the local stiffness of the structure. When the damage occurs, the decrease in stiffness caused by the damage will be directly reflected in the signal changes. In summary, the simulation preliminarily demonstrates the ability of EMI to identify CMSP damage and it is feasible to use DIs for CMSP damage characterization.

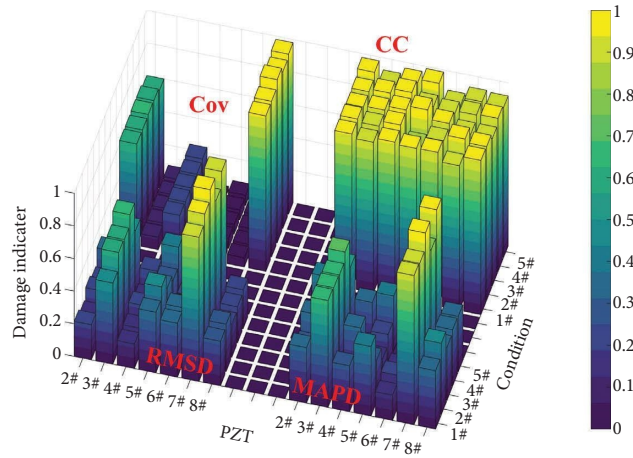


FIGURE 6: DIs of seven PZTs under five damage conditions.

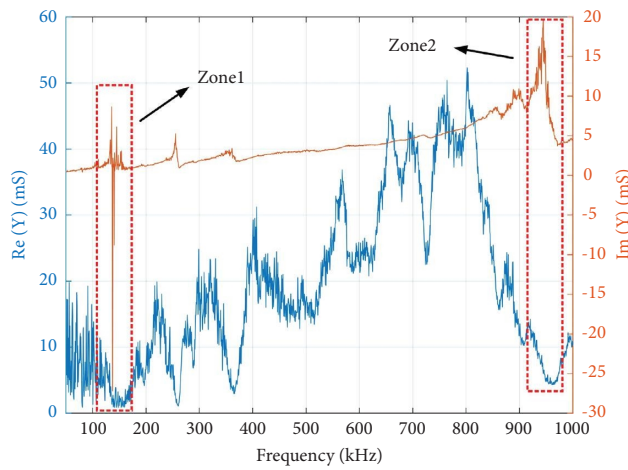
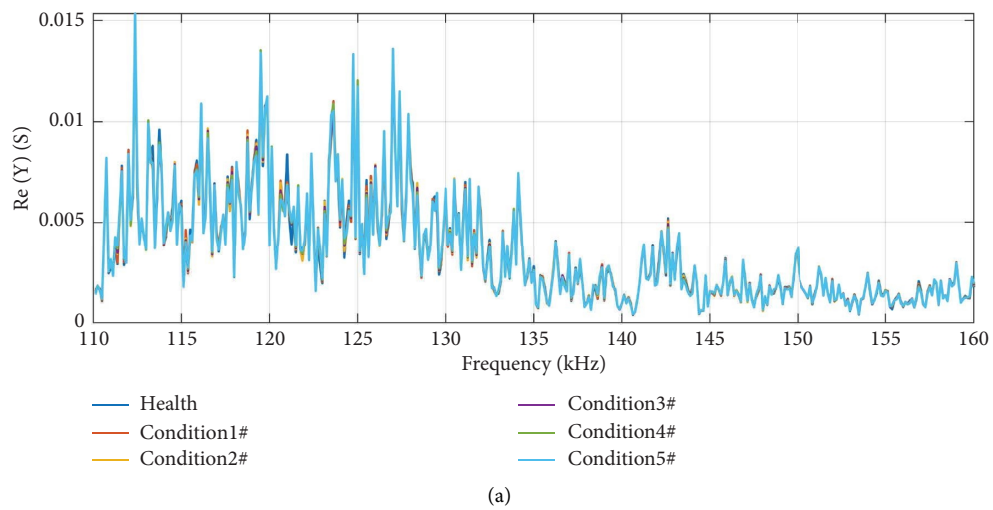


FIGURE 7: The conductance and the susceptance spectra at 50 kHz–1 MHz.



(a)  
FIGURE 8: Continued.



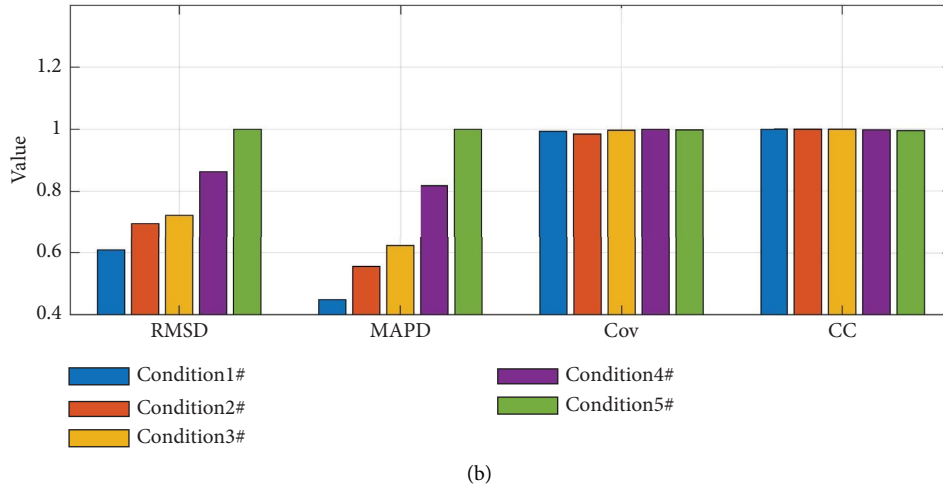


FIGURE 8: The conductance at 110 kHz–160 kHz and DIs under five damage conditions.

#### 4. Experimental Study on Damage Identification of CMSP

Considering the differences between the simulation and experiment, CMSP specimen was made and an experimental platform was built to further verify the applicability of EMI for damage identification of actual CMSP, as shown in Figure 9. The length and width of the CMSP in the experiment are both 825 mm and the geometric dimensions of the stiffeners are consistent with the simulation settings. The signals were collected using the WK6500B precision impedance analyzer. According to the sensor layout in Figure 2(a), eight PZTs were pasted onto CMSP using modified acrylic adhesive with a 1:1 mass ratio of epoxy resin and hardener. To tightly couple the sensor and structure, let it stand for 24 hours after bonding until the epoxy adhesive is completely cured. Positive and negative electrodes on the surface of the PZT are led out and then connected to the fixture of the impedance analyzer during measurement. The upper limit output voltage of 1 V of the analyzer was set as the excitation voltage since the higher excitation voltage in a certain range can significantly improve the detection sensitivity of EMI [31]. Applying additional masses has become a commonly used strategy to introduce reversible discontinuity (damage) in the structure [32]. The magnet can be used to simulate defects as its acoustic impedance is close to that of the specimen [33]. In the experiment, a pair of magnets with a diameter of 12 mm and a thickness of 6 mm was symmetrically placed on the front and back sides of the CMSP. The defects at different positions were simulated by placing the magnets at different positions. The temperature in the laboratory is kept at 26°C and each group is measured 5 times to reduce the impact of random errors on the signal.

**4.1. Study on Quantitative Characterization of Damage Based on DIs.** The admittance spectra of 1#–8# PZT at 50 kHz–1 MHz were obtained before the experiment. The admittance of 1# PZT is shown in Figure 10.

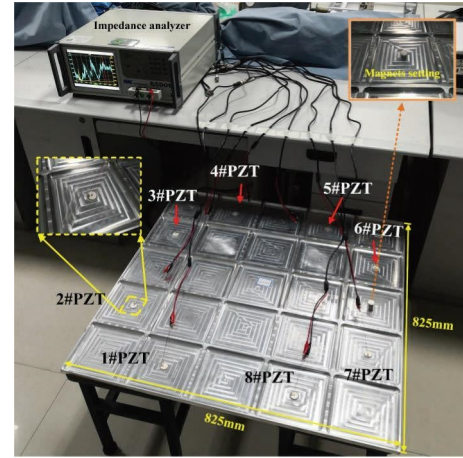


FIGURE 9: The EMI damage detection system.

In Figure 10, there are peaks in the measured susceptance of 1# PZT within the range of 100 kHz–200 kHz and around 900 kHz. The simulated admittance spectrum shows a good agreement with the experimental results in terms of change trend, which verifies the simulation effectiveness. However, an additional resonant peak appeared at 933 kHz (in the black dashed box) in the measured susceptance. The difference may be caused by the deviation between the calibration and the actual parameter of the PZT. After comparing the admittance of eight PZTs, 100 kHz–200 kHz was selected as the frequency range for the study. One to five magnets were attached at the center of the CMSP to simulate five degrees of damage. Then, the benchmark and the signals of damage conditions were obtained. The damage location and the quantification results of five DIs are shown in Figure 11.

Although the damage is set at the center position of 1#–8# PZTs, the indication effects of four DIs at the eight PZTs under five working conditions are different. From an overall perspective, RMSD and MAPD show an increasing trend as the degree of damage increases. Since CC emphasizes the

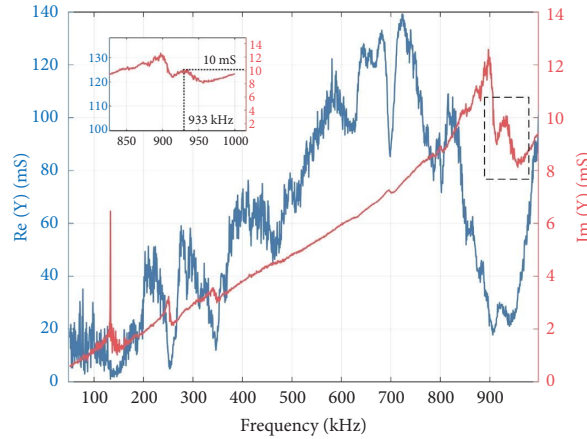


FIGURE 10: The measured conductance and the susceptance spectra at 50 kHz–1 MHz.

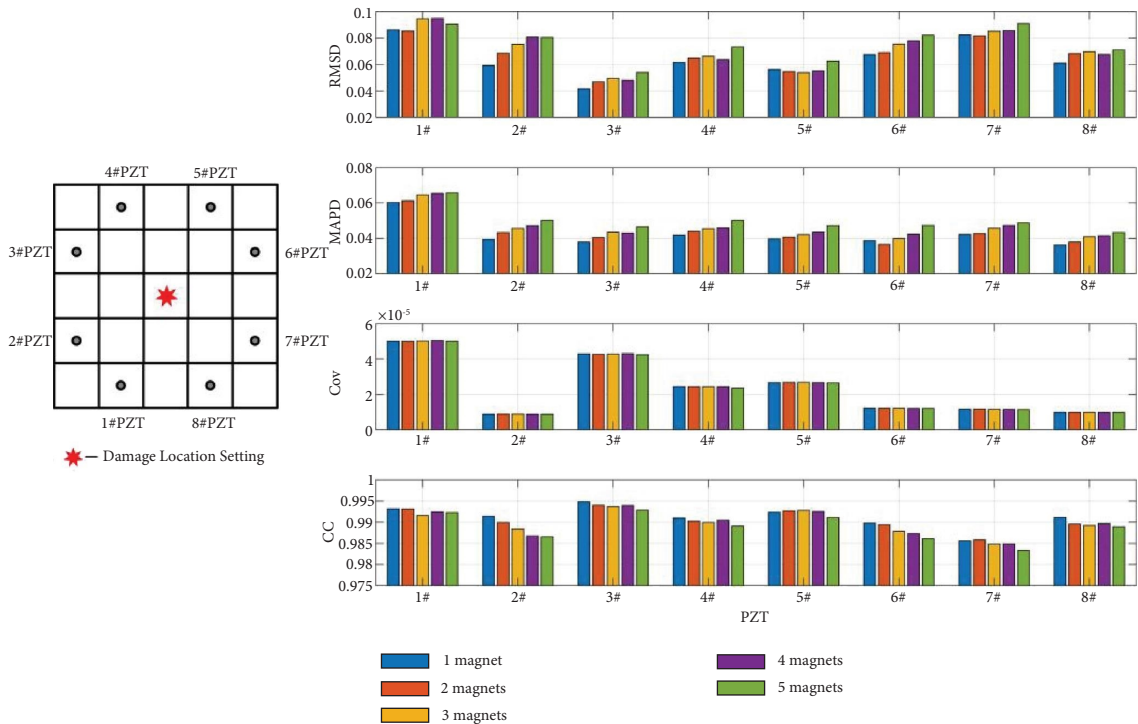


FIGURE 11: DIs in healthy and different severe damage conditions.

correlation between signals, it decreases as the degree of damage increases. Besides, Cov has no significant indicative effect on CMSP damage. As for RMSD and CC, even though they can roughly reflect the degree of damage, there are still inaccuracies in the characterization of adjacent damage conditions. This is due to signal interference caused by noise, resulting in weak indicator ability for minor damage. In addition, for the same damage condition, the ideal value of DI at each PZT should be the same. Taking RMSD at the condition of five magnets as an example, the RMSD variation range of eight PZTs is [0.054, 0.090]. Under the same working condition, the RMSD of different PZTs almost doubled, indicating that RMSD is very sensitive to the performance deviation between sensors and the difference in the adhesive layer. It is not conducive to the construction of a data sample library with RMSD in

practical engineering applications. As for MAPD, it can accurately reflect the degree of damage at the same PZT. On the other hand, except for 1# PZT, MAPD has consistency in indicating values of different PZT for the same damage condition. After the above analysis, MAPD is determined as an indicator to quantify the damage on CMSP.

4.2. Study on Damage Imaging Localization Based on the Modified Probability-Weighted Algorithm. As a mathematical formula, the weighted function appears frequently in statistics and signal processing which is closely relevant to damage detection techniques. Among them, the reconstruction algorithm for probabilistic inspection of defects (RAPID) [34] is a commonly used method for GW damage imaging, which uses the probability-weighted

function to assign more weights to the damaged elements, thus achieving the localization of the damage. In this paper, it is supposed that the DI is linearly related to the Euclidean distance between damage and PZT within the sensing region of the circular PZT. Namely, the DI value of the PZT in the vicinity of damage should be larger than those in far positions. Zhu et al. [35] conducted damage localization based on EMI and probability-weighted ideas. They proposed a method assuming the radius of each PZT sensing area is the same and the detection ability of each PZT is consistent. It is necessary to screen the PZT in advance to ensure that the quality of the sensors used is as close as possible before the experiment. However, the previous results in Section 4.1 demonstrate that the signal is not only affected by the

performance of the sensor itself but also by the quality of the adhesive layer. In practice, it is difficult to ensure complete consistency in the adhesive layer quality, thus the difference in detection ability between sensors cannot be ignored. In addition, as a key algorithm parameter, the sensing area radius must be determined through prior experiments which limits the practical application in engineering.

Drawing on the idea of probability-weighted function, this paper proposes a damage imaging algorithm that takes into account sensor differences without the need to determine the sensing radius in advance. The CMSP is divided into units with a step size of 5 mm, resulting in a total of 165 pixels  $\times$  165 pixels. The estimated probability of damage for each pixel is

$$P(x_i, y_i) = \sum_{k=1}^N [W_k(x_i, y_i) \cdot \text{MAPD}_k], \quad (12)$$

$$W_k(x_i, y_i) = \begin{cases} \left(1 - 0.9 \times \frac{\text{MAPD}_k}{\text{MAPD}_{\max}}\right) \cdot R - \gamma & L_2 = \left(1 - 0.9 \times \frac{\text{MAPD}_k}{\text{MAPD}_{\max}}\right) \cdot R + \gamma, \\ \left[1 - \frac{L_1 - d_k(x_i, y_i)}{L_1}\right] \times \text{Coeff}_k & d_k(x_i, y_i) < L_1, \\ 1 \times \text{Coeff}_k & L_1 \leq d_k(x_i, y_i) \leq L_2, \\ \left[1 - \frac{d_k(x_i, y_i) - L_2}{L_2}\right] \times \text{Coeff}_k & L_2 < d_k(x_i, y_i) \leq 2L_2, \\ 0 & \text{other} \end{cases} \quad (13)$$

where  $N=8$  represents the number of PZT;  $W_k(x_i, y_i)$  denotes the probability of the  $k^{\text{th}}$  PZT on the element  $(x_i, y_i)$ ;  $\text{MAPD}_k$  and  $\text{MAPD}_{\max}$  represents the MAPD of the  $k^{\text{th}}$  PZT signal and the maximum MAPD of all eight sensors, respectively.  $R$  is the distance coefficient from the damage to the sensor. Considering that environmental noise interference can cause small fluctuations in DI near the actual value, redundancy  $\gamma$  is set in the formula.

$d_k(x_i, y_i) = \sqrt{(X_k - x_i)^2 + (Y_k - y_i)^2}$  is the distance from the element to the  $k^{\text{th}}$  PZT,  $(X_k, Y_k)$  represents the horizontal and vertical coordinates of PZT, and  $\text{Coeff}$  is the coefficient of difference between various DIs. By multiplying the  $\text{Coeff}$  with the DI obtained directly from each PZT, it is ensured that under the same damage condition, the DI values of the eight PZTs are the same. Based on the MAPD difference in Figure 11, taking the average MAPD of 2#–8# PZT as the benchmark,  $\text{Coeff}$  was calculated, and  $\text{Coeff} = 0.725, 0.950, 1.023, 0.950, 1.008, 1.007, 0.977, 1.101$ . The schematic diagram of the proposed probability algorithm is shown in Figure 12(a).  $\left[1 - 0.9 \times (\text{MAPD}_k / \text{MAPD}_{\max})\right] \cdot R$  is used to determine the relative distance between the eight PZTs and the damage, which is the origin of the circles with

different radii in Figure 12(a). For ease of illustration, only the imaging states of 3# PZT, 6# PZT, and 8# PZT are shown in Figure 12(a). Taking 1# PZT as an example, when  $R_1 = 160$  mm and  $\delta = 5$  mm, the actual indication effect is shown in Figure 12(b). The further away the pixels on the CMSP are from the points on the circumference, the lower the probability of being judged as the damage. The rule results in two gradually shallower circular areas inside and outside the circle in Figure 12(b) which are controlled by the  $(1 - [L_1 - d_k(x_i, y_i)]/L_1) \times \text{Coeff}_k$  and  $(1 - [d_k(x_i, y_i) - L_2]/L_2) \times \text{Coeff}_k$ , respectively.

In the experiment, the initial value of  $R$  was set to 1, and the iterations were set to 300. During each iteration,  $R$  was incremented by 1. In the initial state, there is no intersection between the imaging circles of each PZT. As  $R$  increases, more and more circles have overlapping areas, and the value of pixels at the damage location increases continuously. Then, the pixel value at the damage reaches its maximum and it is the maximum value not only on all pixels in the CMSP but also in all iterations. As  $R$  further rises, the intersections of the imaging circles increase while they become more dispersed. At the same time, the maximum of the pixels falls down. Therefore, damage can

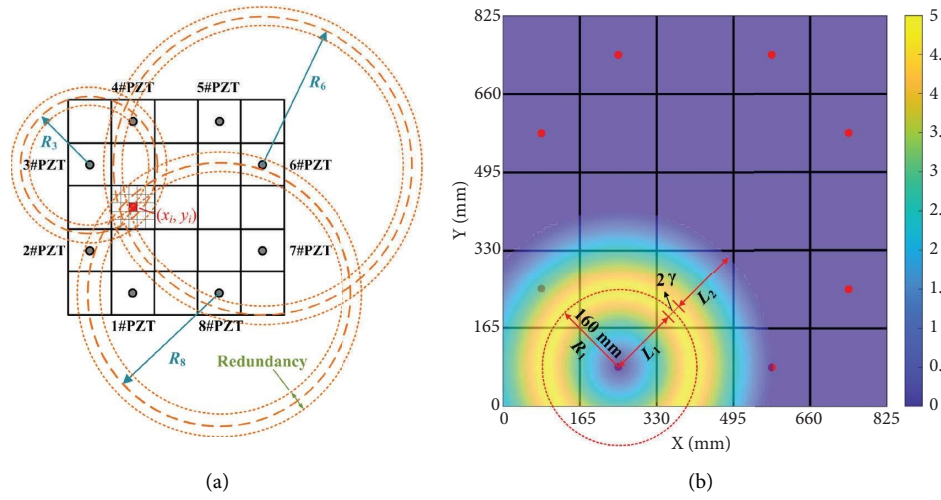


FIGURE 12: Schematic of the modified probability-weighted algorithm.

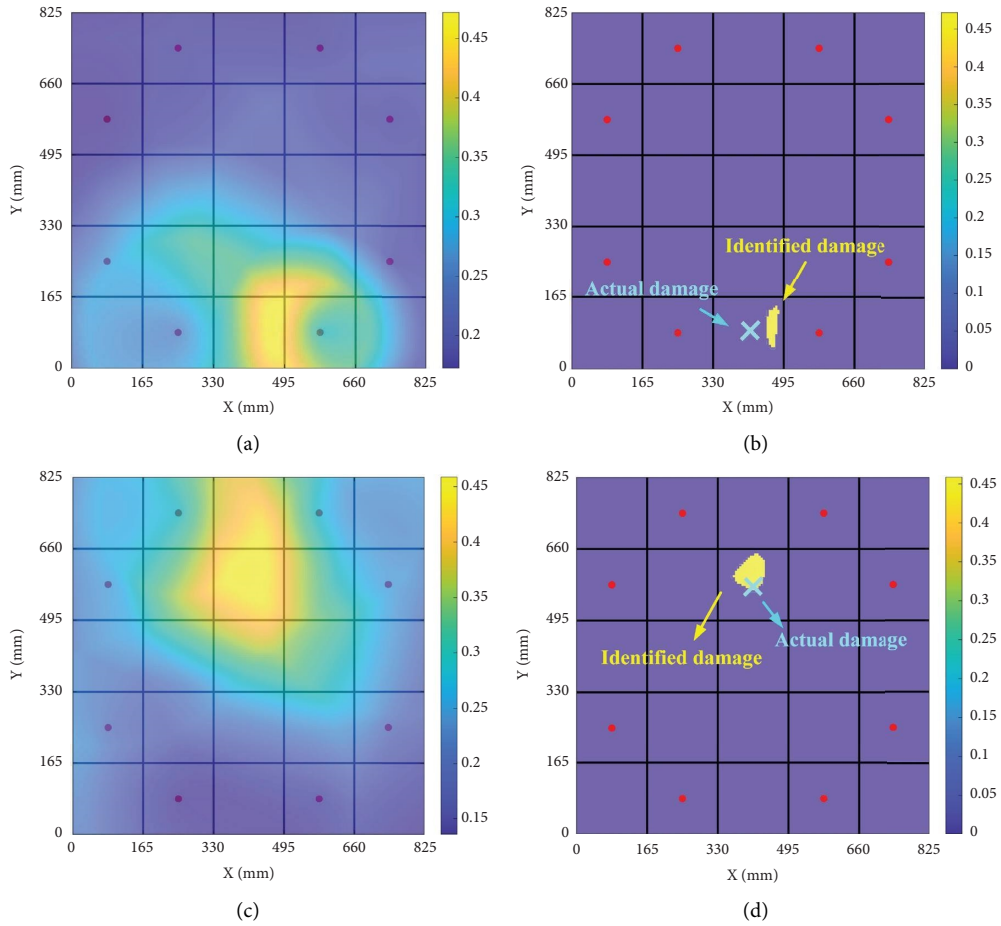


FIGURE 13: Continued.

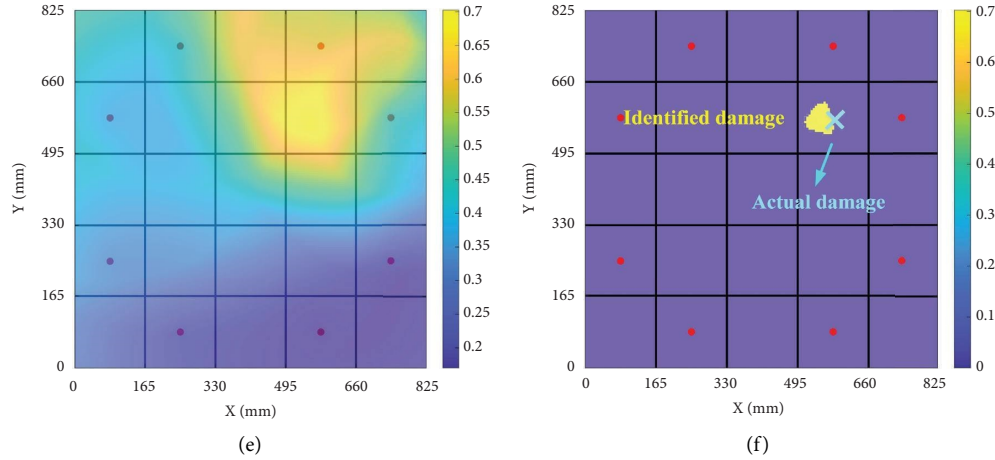


FIGURE 13: Damage identification effect of the modified probability-weighted algorithm.

be located by obtaining the position corresponding to the maximum pixel value within the iterations. Damage was separately set at the region unit of (3,1), (3,4), and (4,4) and then imaged by the proposed algorithm. The maximum value of the pixel was obtained at the 112<sup>nd</sup>, 193<sup>rd</sup>, and 179<sup>th</sup> iterations, respectively. The original imaging effect and the damage identification effect after setting the pixel threshold to 95% of the maximum value are shown in Figure 13.

Figures 13(a), 13(c), and 13(e) represent the original imaging images when the damage is at the region unit of (3,1), (3,4), and (4,4). Figures 13(b), 13(d), and 13(f) respectively represent the recognition position and actual position of the damage. From these three figures, except for a slight deviation between the identified area and the actual damage in the unit (3,1), the other two have achieved accurate damage localization indicating that the imaging method proposed has a good localization effect for CMSP damage.

## 5. Conclusions

GW and EMI are the two main detection methods for active SHM based on piezoelectric ceramics. To achieve damage identification of CMSP, this paper first evaluates the quantification ability of GW and EMI for CMSP damage through finite element analysis. Then, a damage quantification and localization method based on DI and probability-weighted algorithm is proposed and its feasibility is validated by experiment with an actual CMSP specimen. The specific conclusions are as follows:

- (1) Conventional DIs cannot quantitatively identify the CMSP damage of different severities with GW signals as wave reflection and mode conversion occur at the stiffeners which destroy the signal characteristics of the damage. Stiffeners significantly alter the GW propagation path and have an attenuation effect on the propagation energy.
- (2) Different EMI-based DIs have different quantifying abilities for CMSP damage. Among them, MAPD shows a good identification performance as it

accurately characterizes the relative degree of damage while maintaining consistency across different PZTs. As for RMSD and CC, even though they can roughly reflect the damage degree, there are still inaccuracies in the characterization of adjacent damage conditions. Cov is not able to characterize the CMSP damage.

- (3) The proposed probability-weighted damage imaging algorithm takes into account the difference in detection capabilities of PZTs and does not require manual determination of the sensor detection range radius. Damage imaging can be achieved within a few iterations. This algorithm has a great potential for application in actual damage detection of CMSP structures.

The proposed method can realize real-time, online, and continuous health monitoring and early warning, providing strong technical support for the safety management of rocket fuel storage tanks and promoting the intelligence and modernization of aerospace engineering management.

## Data Availability

The data used to support the findings of this study are available from the corresponding author upon request.

## Conflicts of Interest

The authors declare that they have no conflicts of interest.

## Authors' Contributions

Xie Jiang and Wensong Zhou contributed equally to this work.

## Acknowledgments

This research was supported by the National Natural Science Foundation of China (Grant nos. 51975581, 92060106, and 52075541) and the Technology Innovation Team Project of Shaanxi Province (Grant no. 2022TD-62).

## References

- [1] Y. Su, Z. Guan, X. Wang, Z. Li, J. Guo, and Y. Huang, "Buckling and post-buckling behavior of titanium alloy stiffened panels under shear load," *Chinese Journal of Aeronautics*, vol. 32, no. 3, pp. 619–626, 2019.
- [2] Z. Yu, C. Xu, J. Sun, and F. Du, "Guided wave propagation analysis in stiffened panel using time-domain spectral finite element method," *Chinese Journal of Aeronautics*, vol. 35, no. 10, pp. 208–221, 2022.
- [3] C. Meeks, E. Greenhalgh, and B. G. Falzon, "Stiffener debonding mechanisms in post-buckled CFRP aerospace panels," *Composites Part A: Applied Science and Manufacturing*, vol. 36, no. 7, pp. 934–946, 2005.
- [4] M. Tang, X. Wu, M. Cong, and K. Guo, "A method based on SVD for detecting the defect using the magnetostrictive guided wave technique," *Mechanical Systems and Signal Processing*, vol. 70–71, pp. 601–612, 2016.
- [5] T. Wandowski, P. H. Malinowski, and W. M. Ostachowicz, "Circular sensing networks for guided waves based structural health monitoring," *Mechanical Systems and Signal Processing*, vol. 66–67, pp. 248–267, 2016.
- [6] F. Ricci, E. Monaco, L. Maio, N. D. Boffa, and A. K. Mal, "Guided waves in a stiffened composite laminate with a delamination," *Structural Health Monitoring*, vol. 15, no. 3, pp. 351–358, 2016.
- [7] C. Ramadas, K. Balasubramaniam, M. Joshi, and C. V. Krishnamurthy, "Interaction of Lamb mode (Ao) with structural discontinuity and generation of "Turning modes" in a T-joint," *Ultrasonics*, vol. 51, no. 5, pp. 586–595, 2011.
- [8] M. Faisal Haider, M. Y. Bhuiyan, B. Poddar, B. Lin, and V. Giurgiutiu, "Analytical and experimental investigation of the interaction of Lamb waves in a stiffened aluminum plate with a horizontal crack at the root of the stiffener," *Journal of Sound and Vibration*, vol. 431, pp. 212–225, 2018.
- [9] R. S. Reusser, S. D. Holland, D. E. Chimenti, and R. A. Roberts, "Reflection and transmission of guided ultrasonic plate waves by vertical stiffeners," *Journal of the Acoustical Society of America*, vol. 136, no. 1, pp. 170–182, 2014.
- [10] C. R. Bijudas, M. Mitra, and P. M. Mujumdar, "Time reversed Lamb wave for damage detection in a stiffened aluminum plate," *Smart Materials and Structures*, vol. 22, no. 10, p. 105026, 2013.
- [11] C. Schaal and A. Mal, "Lamb wave propagation in a plate with step discontinuities," *Wave Motion*, vol. 66, pp. 177–189, 2016.
- [12] B. A. De Castro, F. G. Baptista, and F. Ciampa, "Comparative analysis of signal processing techniques for impedance-based SHM applications in noisy environments," *Mechanical Systems and Signal Processing*, vol. 126, pp. 326–340, 2019.
- [13] W. Li, T. Liu, D. Zou, J. Wang, and T.-H. Yi, "PZT based smart corrosion coupon using electromechanical impedance," *Mechanical Systems and Signal Processing*, vol. 129, pp. 455–469, 2019.
- [14] J. Wu, Y. Chen, J. Wang, Z. Liu, and W. Li, "Electromechanical impedance instrumented wearable piezoelectric ring-type sensor for bolted connection monitoring," *IEEE Sensors Journal*, vol. 23, no. 13, pp. 14872–14881, 2023.
- [15] F. Du, S. Wu, C. Xu, Z. Yang, and Z. Su, "Electromechanical impedance temperature compensation and bolt loosening monitoring based on modified unet and multitask learning," *IEEE Sensors Journal*, vol. 23, no. 5, pp. 4556–4567, 2023.
- [16] D. Ai and J. Cheng, "A deep learning approach for electromechanical impedance based concrete structural damage quantification using two-dimensional convolutional neural network," *Mechanical Systems and Signal Processing*, vol. 183, 2023.
- [17] G. Li, M. Luo, J. Huang, and W. Li, "Early-age concrete strength monitoring using smart aggregate based on electromechanical impedance and machine learning," *Mechanical Systems and Signal Processing*, vol. 186, 2023.
- [18] D. Ai, F. Mo, J. Cheng, and L. Du, "Deep learning of electromechanical impedance for concrete structural damage identification using 1-D convolutional neural networks," *Construction and Building Materials*, vol. 385, 2023.
- [19] X. Fu, W. Li, L. Li, J. Wang, B. Lu, and J. Wu, "Cloud-based pipe corrosion monitoring using electromechanical impedance instrumented piezoelectric ring sensor," *Automation in Construction*, vol. 156, 2023.
- [20] J. Zhu, J. Wen, Z. Han et al., "Impact energy assessment of sandwich composites using an ensemble approach boosted by deep learning and electromechanical impedance," *Smart Materials and Structures*, vol. 32, no. 9, 2023.
- [21] W. Zhou, H. Li, and F.-G. Yuan, "Fundamental understanding of wave generation and reception using d36 type piezoelectric transducers," *Ultrasonics*, vol. 57, pp. 135–143, 2015.
- [22] Y. Yang, J. Xu, and C. K. Soh, "Generic impedance-based model for structure-piezoceramic interacting system," *Journal of Aerospace Engineering*, vol. 18, no. 2, pp. 93–101, 2005.
- [23] Y. Zhang, F. Xu, T. Zhang, L. Ma, and C. Wu, "Electromechanical impedance modeling for health monitoring of a damaged thin plate," in *Proceedings of the 2011 3rd International Conference on Measuring Technology and Mechatronics Automation, Shanghai*, January 2011.
- [24] T. Monnier, "Lamb waves-based impact damage monitoring of a stiffened aircraft panel using piezoelectric transducers," *Journal of Intelligent Material Systems and Structures*, vol. 17, no. 5, pp. 411–421, 2006.
- [25] J. Li, Y. Lu, and H. Ma, "Linear and nonlinear guided wave based debonding monitoring in CFRP-reinforced steel structures," *Construction and Building Materials*, vol. 400, 2023.
- [26] S. Park, J.-W. Kim, C. Lee, and S.-K. Park, "Impedance-based wireless debonding condition monitoring of CFRP laminated concrete structures," *NDT and E International*, vol. 44, no. 2, pp. 232–238, 2011.
- [27] R. Tawie and H. K. Lee, "Monitoring the strength development in concrete by EMI sensing technique," *Construction and Building Materials*, vol. 24, no. 9, pp. 1746–1753, 2010.
- [28] J. Min, S. Park, and C.-B. Yun, "Impedance-based structural health monitoring using neural networks for autonomous frequency range selection," *Smart Materials and Structures*, vol. 19, no. 12, 2010.
- [29] T.-C. Huynh and J.-T. Kim, "Quantification of temperature effect on impedance monitoring via PZT interface for prestressed tendon anchorage," *Smart Materials and Structures*, vol. 26, no. 12, 2017.
- [30] W. Yan and W. Q. Chen, "Structural health monitoring using high-frequency electromechanical impedance signatures," *Advances in Civil Engineering*, vol. 2010, pp. 1–11, 2010.
- [31] Y. Hu and Y. Yang, "Wave propagation modeling of the PZT sensing region for structural health monitoring," *Smart Materials and Structures*, vol. 16, no. 3, pp. 706–716, 2007.
- [32] R. Soman, "Sequential niching particle swarm optimization algorithm for localization of multiple damage locations using fiber Bragg grating sensors," *NDT and E International*, vol. 143, 2024.

- [33] S. Xue, W. Zhou, J. L. Beck, Y. Huang, and H. Li, "Damage localization and robust diagnostics in guided-wave testing using multitask complex hierarchical sparse Bayesian learning," *Mechanical Systems and Signal Processing*, vol. 197, 2023.
- [34] M. Tabatabaeipour, J. Hettler, S. Delrue, and K. V. D. Abeeel, "reconstruction algorithm for probabilistic inspection of damage (RAPID) in composites," in *Proceedings of the 11th European Conference on Non-Destructive Testing (ECNDT 2014)*, Prague, Czech Republic, October 2014.
- [35] J. Zhu, X. Qing, X. Liu, and Y. Wang, "Electromechanical impedance-based damage localization with novel signatures extraction methodology and modified probability-weighted algorithm," *Mechanical Systems and Signal Processing*, vol. 146, 2021.